

Microscopic many-body theory of two-dimensional coherent spectroscopy of excitons and trions in atomically thin transition metal dichalcogenides

Hui Hu,¹ Jia Wang,¹ and Xia-Ji Liu¹

¹*Centre for Quantum Technology Theory, Swinburne University of Technology, Melbourne 3122, Australia*
(Dated: August 9, 2022)

We present a microscopic many-body theory of the recently measured two-dimensional coherent spectroscopy (2DCS) of excitons and trions in monolayer MoSe₂ materials [K. Hao *et al.*, Nano Lett. **16**, 5109 (2016)], where excitons and trions can be well interpreted as repulsive and attractive polarons, respectively, in the dilute limit of exciton density. We derive a simple relation for the 2DCS spectrum in terms of a modified, mixing time-dependent polaron Green function, which is valid in the single exciton limit. Our simulated spectra are in excellent qualitative agreement with experiments without introducing any phenomenological parameters such as decoherence rates. In particular, quantum beats between the off-diagonal crosspeaks in the experimental 2DCS spectra are well reproduced. Our work, therefore, clarifies the microscopic principle that underlies the observed optical signals of exciton-trion coherence. We find that there are two quantitative discrepancies between theory and experiment: the smaller than expected crosspeak strength and the slightly unsynchronized quantum beats at different crosspeaks. Tentatively, we attribute these residual discrepancies to the finite exciton density and the resultant polaron-polaron interaction, which is not taken into account in our theory.

I. INTRODUCTION

Over the last decade, atomically thin transition metal dichalcogenides (TMD) have received increasing attention^{1–3} due to their unique physical properties arising from extreme low-dimensional constraints. These two-dimensional (2D) materials are expected to be promising candidates for a wide range of applications in ultrathin low-power electronics, optoelectronics, and spintronics. For this perspective, different types of experimental spectroscopy techniques have been used to characterize optical properties of monolayer TMD materials^{2,3}, including the reflection or absorption spectra⁴, photoluminescence⁵, nonlinear two-pulse pump-probe measurement^{6,7}, and nonlinear four-wave-mixing⁸.

Here, we are specifically interested in the nonlinear two-dimensional coherent spectroscopy (2DCS) based on the four-wave-mixing^{9–11}, which enables the study of excited-state dynamics on femtosecond (fs) timescales and maps out the full third-order nonlinear optical susceptibility of 2D materials by correlating excitation and emission energies¹¹. 2DCS has been applied to probe the formation and dynamics of excitons and higher-order excitonic complexes such as trions and bi-excitons in both molybdenum-based (MoX₂) and tungsten-based (WX₂) TMD materials^{8,12–14}. A remarkable recent experimental discovery is the quantum coherence between trions and excitons in monolayer MoSe₂, as revealed by quantum beats between the two off-diagonal crosspeaks at the timescale of 100 fs¹². However, due to the lack of theoretical interpretation of 2DCS spectrum at the microscopic level¹⁰, it remains a challenge to clarify the microscopic mechanisms underlying such quantum beats.

In this respect, two pioneering theoretical analyses are worth mentioning^{15,16}. One is the combined use of the

perturbative Fermi golden rule and the few-body solution for excitons and trions by Tempelaar and Berkelbach¹⁵. As in the experiment, the electron density could be nonzero, a trion is now commonly viewed as an attractive polaron^{17,18}, i.e., a quasiparticle formed by dressing an exciton with particle-hole excitations of the electron Fermi sea^{19–22}. Therefore, in the numerical calculations for three-body trions¹⁵, the Brillouin zone sampling resolution has been varied as a way to effectively tune the electron density and to provide an approximate polaron description for excitons and trions. In another theoretical analysis by Lindoy, Chang, and Reichman¹⁶, which was posted most recently, the unrealistic limit of an infinitely heavy hole has been taken in order to utilize the exact solution of the well-known Mahan-Nozières-De Dominicis (MND) model^{23–25}. However, in the immobile heavy hole limit, polaron quasiparticle resonance turns into a power-law singularity due to the famous Anderson Anderson’s orthogonality catastrophe^{26,27}. Although the MND model provides useful insight into quantum beats, it is desirable to consider mobile holes and excitons with finite mass.

In this work, we would like to remove the downsides of these two theoretical analyses by taking an *exact* polaron model for *mobile* excitons and trions, with a realistic exciton mass. We present a full microscopic many-body calculation of the 2DCS spectrum of excitons and trions. Intriguingly, as photons in four-wave-mixing pulses have negligible momentum²⁵, any intermediate non-exciton states that involve particle-hole excitations of the Fermi sea will not make contributions to the 2DCS signal due to their different linear momentum from the initial configuration of the electron Fermi sea. This is true if we always restrict the maximum number of exciton during excitations to one in the low exciton density limit. The absence of particle-hole excitations allows us to derive a simple expression for the 2DCS spectrum, which provides a mi-

microscopic understanding of the perturbative Fermi golden rule adopted by Tempelaar and Berkelbach¹⁵. The latter was adopted without explanation.

We perform a numerical simulation of the 2DCS spectrum under the experimental conditions without introducing any phenomenological parameters. There are excellent qualitative agreements between our theory and the recent experiment by Hao *et al.*¹², indicating that the microscopic mechanism of quantum beats is indeed captured by the exciton-trion-polaron model^{17,18}. We also find some residual discrepancies, such as the smaller than expected crosspeak strength and the slightly unsynchronized oscillations at different crosspeaks. These discrepancies could be due to the polaron-polaron interaction at finite exciton density, which is not considered in our calculations but is worth exploring in future works.

It is interesting to note that a cold-atom analog of the 2DCS spectroscopy was recently proposed by us (i.e., the 2D Ramsey spectroscopy)^{28,29}, in which the role of an exciton is played by a spin-1/2 impurity atom, and the four-wave-mixing is implemented by using a sequence of Ramsey $\pi/2$ radio-frequency (rf) pulses to flip the pseudospin of the impurity²⁷. In this work, we will also briefly compare the two different two-dimensional spectroscopy.

The rest of the paper is organized as follows. In the following section (Sec. II), we outline the model Hamiltonian for the exciton-trion-polaron in 2D materials. In Sec. III, we present the many-body theory of the 2DCS spectroscopy and make a brief comparison to the 2D Ramsey spectroscopy with cold-atoms²⁹. In Sec. IV, we first discuss the details of our numerical calculations and then show the theoretical results in comparison with the experimental data¹². Finally, Sec. V is devoted to conclusions and outlooks.

II. MODEL HAMILTONIAN

In monolayer MoSe₂, spin-up (spin-down) electrons and holes near the K (K') valley can form tightly bound excitons, with binding energy about several hundred meV^{2,12}. These excitons can also attract extra spin-opposite electrons (to be described by the creation and annihilation field operators $c_{\mathbf{k}}^\dagger$ and $c_{\mathbf{k}}$) in other valley to form singlet trions, with a trion binding energy $E_T \sim 30$ meV¹⁵. In general, the density of extra electrons in other valley is finite, as characterized by an electron Fermi energy about several ten meV, $\varepsilon_F \sim 10$ meV. As the exciton binding energy is significantly larger than other energy scales in the system, the internal structure of excitons is frozen and we can describe them by using the creation and annihilation field operators $X_{\mathbf{k}}^\dagger$ and $X_{\mathbf{k}}$. In the dilute limit of exciton density, the system under consideration therefore can be well described by a polaron model

Hamiltonian ($\hbar = 1$)^{17,18},

$$\mathcal{H} = \sum_{\mathbf{k}} \left[\epsilon_{\mathbf{k}} c_{\mathbf{k}}^\dagger c_{\mathbf{k}} + \epsilon_{\mathbf{k}}^X X_{\mathbf{k}}^\dagger X_{\mathbf{k}} \right] + U \sum_{\mathbf{q}, \mathbf{k}, \mathbf{p}} X_{\mathbf{k}}^\dagger c_{\mathbf{q}-\mathbf{k}}^\dagger c_{\mathbf{q}-\mathbf{p}} X_{\mathbf{p}}, \quad (1)$$

where the maximum number of exciton is restricted to 1, i.e., $\sum_{\mathbf{k}} X_{\mathbf{k}}^\dagger X_{\mathbf{k}} \leq 1$, and the density of the electrons ($n = \sum_{\mathbf{k}} c_{\mathbf{k}}^\dagger c_{\mathbf{k}}$) can be tuned by the Fermi energy ε_F through gate voltage. $\epsilon_{\mathbf{k}} = k^2/(2m_e)$ and $\epsilon_{\mathbf{k}}^X = k^2/(2m_X)$ are the single-particle energy dispersion relation of electrons and excitons, respectively, with electron mass m_e and exciton mass $m_X \simeq 2m_e$ in 2D TMD materials².

In the dilute limit of electron density ($n \rightarrow 0$), the formation of a trion is driven by the interaction Hamiltonian (i.e., the U -term). Hence, the interaction strength U can be determined by reproducing the trion binding energy E_T ^{17,18}. In the general case of a finite electron density, it is now understood that trions and excitons could be well interpreted as the attractive polarons and repulsive polarons, the two types of quasiparticles that have been systematically studied over the past fifteen years in ultracold atomic physics^{19–22}.

III. MANY-BODY THEORY OF TWO-DIMENSIONAL COHERENT SPECTROSCOPY

In the 2DCS spectroscopy^{9,10}, three pulses are applied to the sample at times τ_1 , τ_2 and τ_3 , respectively, separated by an evolution time delay $t_1 = \tau_2 - \tau_1$ and a mixing time delay $t_2 = \tau_3 - \tau_2$, as illustrated in Fig. 1(a). The nonlinear third-order four-wave-mixing signal (i.e., the red wave-packet in the figure), as a result of the three pulses, is measured with frequency-domain heterodyne detection at a later time τ_s , separated from the third pulse by an emission time delay $t_3 = \tau_s - \tau_3$. In the 2DCS experiment for excitons and trions in MoSe₂¹², the three excitation pulses and detected signal are all co-circularly polarized (i.e., σ^+ polarization). As a consequence, only K -valley excitons are created or annihilated by each excitation pulse, as described by the light-matter interaction operator \hat{V} ,

$$\sum_{\mathbf{k}} \left(\phi_{\mathbf{k}} e_{\mathbf{k}} h_{-\mathbf{k}} + \phi_{\mathbf{k}}^* h_{-\mathbf{k}}^\dagger e_{\mathbf{k}}^\dagger \right) \propto X_0 + X_0^\dagger \equiv \hat{V}, \quad (2)$$

where $\phi_{\mathbf{k}}$ is the dipole matrix element. As we mentioned earlier, the proportionality in the above equation (i.e., the introduction of the exciton field operator) is reasonable in the limit of extremely large exciton binding energy. We note that, only the zero-momentum exciton field operators appear in the interaction operator \hat{V} , due to the negligible photon momentum in the excitation pulses (i.e., $\mathbf{k}_i \sim \mathbf{k}_s \sim 0$). After some of the three pulses, different many-body polaron states $|e\rangle$ with a single exciton are created. These include the inter-valley trion or attractive polaron, consisting of a K -valley exciton and a

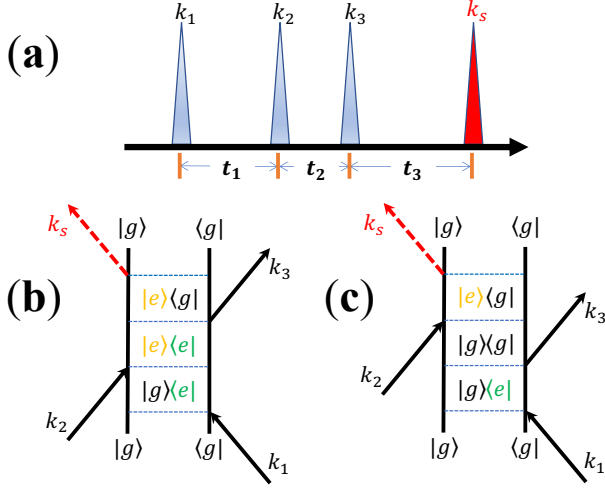


FIG. 1. (a) Time ordering of excitation pulses for standard rephasing 2D coherent spectra. The evolution, mixing, and emission time delays are labeled as t_1 , t_2 , and t_3 , respectively. (b) and (c): The two double-sided Feynman diagrams representing the two contributions to the phase-match directions, $\mathbf{k}_s = -\mathbf{k}_1 + \mathbf{k}_2 + \mathbf{k}_3$. (b) describes the process of excited-state emission (ESE), $R_2(t_1, t_2, t_3)$, while (c) is referred to as ground-state bleaching (GSB), $R_3(t_1, t_2, t_3)$. Here, we use $|g\rangle$ and $|e\rangle$ to denote the many-body states without and with excitons, respectively. There could be infinitely many excited many-body (polaron) states $|e\rangle$, as indicated by different colors. In contrast, the many-body state of the electron gas $|g\rangle$ (describing the Fermi sea) does not change, due to the negligible momentum of photons in the excitation pulses, as discussed in the text.

K' -valley electron, dressed by the multiple-particle-hole excitations of the electron Fermi sea in the K' -valley^{12,15}.

According to the standard nonlinear response theory^{11,30,31}, the four-wave-mixing signal is given by the third-order nonlinear response function,

$$\mathcal{R}^{(3)} \propto \left\langle \left[\left[\left[\hat{V}(t_1 + t_2 + t_3), \hat{V}(t_1 + t_2) \right], \hat{V}(t_1) \right], \hat{V} \right] \right\rangle, \quad (3)$$

where the time-dependent interaction operator $\hat{V}(t) \equiv e^{i\mathcal{H}t} \hat{V} e^{-i\mathcal{H}t}$, and $\langle \dots \rangle$ stands for the quantum average over the initial many-body configuration of the system without excitation pulses, which can be either the ground

state at zero temperature or a thermal state at nonzero temperature. By expanding the three bosonic commutators, there are a total of four distinct correlation functions and their complex conjugates¹¹. For the rephasing scheme (i.e., $t_1 > 0$) with the phase-match directions, $\mathbf{k}_s = -\mathbf{k}_1 + \mathbf{k}_2 + \mathbf{k}_3$, as adopted in the experiment¹², we can consider two significant contributions within the rotating-wave-approximation in the low exciton density limit, i.e., the process of so-called excited-state emission (ESE)^{13,31},

$$R_2 = \left\langle \hat{V} \hat{V}(t_1 + t_2) \hat{V}(t_1 + t_2 + t_3) \hat{V}(t_1) \right\rangle, \quad (4)$$

and the process of ground-state bleaching (GSB)^{13,31},

$$R_3 = \left\langle \hat{V} \hat{V}(t_1) \hat{V}(t_1 + t_2 + t_3) \hat{V}(t_1 + t_2) \right\rangle. \quad (5)$$

These two processes can be understood by using double-sided Feynman diagrams, as shown in Fig. 1(b) and Fig. 1(c), respectively. Note that, at a small exciton density we only include the excitations involving a *single* exciton and therefore neglect the third rephasing process of excited-state absorption (ESA)^{13,31}, $R_1^*(t_1, t_2, t_3)$.

The total rephasing 2DCS spectrum can then be obtained by evaluating the two correlation functions after a double Fourier transformation^{10,31},

$$\mathcal{S}(\omega_1, t_2, \omega_3) = \mathcal{S}_2(\omega_1, t_2, \omega_3) + \mathcal{S}_3(\omega_1, t_2, \omega_3), \quad (6)$$

where for $i = 2, 3$,

$$\mathcal{S}_i = \int_0^\infty \int_0^\infty dt_1 dt_3 e^{i\omega_1^+ t_1} e^{i\omega_3^+ t_3} R_i(t_1, t_2, t_3). \quad (7)$$

Here, ω_1 is the excitation (or absorption) energy and ω_3 is the emission energy. As a response function, we have defined $\omega_1^+ = \omega_1 + i0^+$ and $\omega_3^+ = \omega_3 + i0^+$, where the infinitesimal 0^+ is introduced to regularize the Fourier transformation at $t_1 \rightarrow \infty$ and $t_3 \rightarrow \infty$.

A. A simple expression of the 2DCS spectrum

Let us first focus on the ESE process, $R_2(t_1, t_2, t_3)$, as described by Fig. 1(b). By inserting the expression of \hat{V}_0 and explicitly listing the time-dependence of the operators, we find that,

$$R_2(t_1, t_2, t_3) = \langle \text{FS} | X_0 e^{i\mathcal{H}_X(t_1+t_2)} X_0^\dagger e^{i\mathcal{H}_0 t_3} X_0 e^{-i\mathcal{H}_X(t_2+t_3)} X_0^\dagger | \text{FS} \rangle e^{-iE_{\text{FS}} t_1}, \quad (8)$$

where \mathcal{H}_0 and \mathcal{H}_X denote the model Hamiltonian \mathcal{H} in the cases of no exciton and of a single exciton, respectively. We also denote the initial configuration of the system (without any excitons and with a background en-

ergy E_{FS} of the electron Fermi sea) as $|\text{FS}\rangle$, so we can evaluate

$$e^{-i\mathcal{H}t_1} |\text{FS}\rangle = e^{-i\mathcal{H}_0 t_1} |\text{FS}\rangle = e^{-iE_{\text{FS}} t_1} |\text{FS}\rangle. \quad (9)$$

The configuration $|\text{FS}\rangle$ could be a thermal mixed state at nonzero temperature.

In the above expression of $R_2(t_1, t_2, t_3)$, we may insert a complete set of many-body states of the electron Fermi sea, just before or just after $e^{i\mathcal{H}_0 t_3}$. These many-body states can formally be constructed by creating multiple-particle-hole excitations out of the Fermi sea, in the form,

$$|\vec{\kappa}_\nu\rangle = \left[\prod_{i=1}^{\nu} c_{\mathbf{k}_p^{(i)}}^\dagger \prod_{i=1}^{\nu} c_{\mathbf{k}_h^{(i)}} \right] |\text{FS}\rangle, \quad (10)$$

where ν is the number of particle-hole pairs, $\vec{\kappa}_\nu \equiv \{\mathbf{k}_p^{(1)}, \mathbf{k}_p^{(2)}, \dots, \mathbf{k}_p^{(\nu)}; \mathbf{k}_h^{(1)}, \mathbf{k}_h^{(2)}, \dots, \mathbf{k}_h^{(\nu)}\}$ collectively indexes the ν particle momenta ($\mathbf{k}_p^{(i)} > k_F$) and hole momenta ($\mathbf{k}_h^{(i)} < k_F$), where k_F is the Fermi wavevector. The corresponding momentum and energy of the many-body state can be denoted as $\epsilon_{\vec{\kappa}_\nu}$ and $\mathbf{k}_{\vec{\kappa}_\nu}$, respectively. In the absence of any particle-hole excitations, we simply have $|\vec{\kappa}_{\nu=0}\rangle = |\text{FS}\rangle$ and $\epsilon_{\vec{\kappa}_\nu} = E_{\text{FS}}$.

By inserting the identity $\sum_{\vec{\kappa}_\nu} |\vec{\kappa}_\nu\rangle \langle \vec{\kappa}_\nu| = 1$ into Eq. (8), we find that,

$$R_2 = \sum_{\vec{\kappa}_\nu} F_{\vec{\kappa}_\nu}^* (t_1 + t_2) F_{\vec{\kappa}_\nu} (t_2 + t_3) e^{i\epsilon_{\vec{\kappa}_\nu} t_3} e^{-iE_{\text{FS}} t_1}, \quad (11)$$

where we have defined the correlation function,

$$F_{\vec{\kappa}_\nu} (t) \equiv \langle \vec{\kappa}_\nu | X_0 e^{-i\mathcal{H}_X t} X_0^\dagger | \text{FS} \rangle. \quad (12)$$

An immediate observation is that, as a result of the momentum conservation, the many-body states $|\vec{\kappa}_\nu\rangle$ must have *zero* momentum. Thus, no particle-hole excitations are allowed in $|\vec{\kappa}_\nu\rangle$ and the only contribution to $F_{\vec{\kappa}_\nu}(t)$ is provided by the unperturbed Fermi sea, $|\vec{\kappa}_{\nu=0}\rangle = |\text{FS}\rangle$.

We now see that the correlation function $F_{\vec{\kappa}_\nu}(t)$ can be directly expressed in terms of the retarded polaron Green function at zero momentum $G_{\mathbf{k}=0}(t) = G(t)$, i.e.,

$$F(t) = iG(t) e^{-iE_{\text{FS}} t}, \quad (13)$$

where²⁵

$$G_{\mathbf{k}}(t - t') \equiv -i\theta(t - t') \langle \text{FS} | [X_{\mathbf{k}}(t), X_{\mathbf{k}}^\dagger(t')] | \text{FS} \rangle. \quad (14)$$

Therefore, we obtain a remarkably simple expression for the ESE contribution R_2 ,

$$R_2(t_1, t_2, t_3) = G^*(t_1 + t_2) G(t_2 + t_3). \quad (15)$$

It would be useful to write down a formal expression for the retarded polaron Green function at zero momentum. For this purpose, we recall that different zero-momentum polaron states (i.e., the n -th state with polaron energy $E^{(n)}$) can be written as^{29,32},

$$|n\rangle = \phi_0^{(n)} X_0^\dagger |\text{FS}\rangle + \sum_{\vec{\kappa}_\nu \geq 1} \phi_{\vec{\kappa}_\nu}^{(n)} X_{-\mathbf{k}_{\vec{\kappa}_\nu}}^\dagger |\vec{\kappa}_\nu\rangle, \quad (16)$$

where the second term describes the dressing of multi-particle-hole excitations and the first term describes the ability of free propagation of the exciton, as measured by the polaron residue $Z^{(n)} \equiv \phi_0^{(n)*} \phi_0^{(n)}$. By inserting the identity

$$e^{-i\mathcal{H}_X t} = \sum_n |n\rangle e^{-iE^{(n)} t} \langle n| \quad (17)$$

into the expression of the polaron Green function, we find that,

$$G(t) = -i \sum_n Z^{(n)} e^{-i\mathcal{E}^{(n)} t}, \quad (18)$$

where $\mathcal{E}^{(n)} = E^{(n)} - E_{\text{FS}}$ is the polaron energy measured with respect to the Fermi sea energy. Therefore, the ESE contribution R_2 takes the form,

$$R_2 = \sum_{nm} Z^{(n)} Z^{(m)} e^{i\mathcal{E}^{(n)} t_1} e^{i[\mathcal{E}^{(n)} - \mathcal{E}^{(m)}] t_2} e^{-i\mathcal{E}^{(m)} t_3}. \quad (19)$$

The physics behind this expression may easily be understood from the ESE process illustrated in Fig. 1(b). The factor $Z^{(n)} Z^{(m)}$ or $\phi_0^{(n)} \phi_0^{(m)*} \phi_0^{(m)} \phi_0^{(n)*}$ measures the transfer rates between many-body states induced by the three excitation pulses and the four-wave-mixing signal, while the three dynamical (time-evolution) phase factors simply show the phases accumulated during the time delays t_1 , t_2 and t_3 , respectively.

After the double Fourier transformation, we obtain

$$\mathcal{S}_2 = \sum_{nm} \frac{-Z^{(n)}}{\omega_1^+ + \mathcal{E}^{(n)}} e^{i[\mathcal{E}^{(n)} - \mathcal{E}^{(m)}] t_2} \frac{Z^{(m)}}{\omega_3^+ - \mathcal{E}^{(m)}}. \quad (20)$$

It is convenient to introduce a modified, t_2 -dependent polaron Green function in the frequency domain²⁵,

$$G_R(\omega, t_2) \equiv \sum_n \frac{Z^{(n)}}{\omega + i0^+ - \mathcal{E}^{(n)}} e^{-i\mathcal{E}^{(n)} t_2}, \quad (21)$$

which reduces to the conventional retarded polaron Green function $G_R(\omega)$ at zero mixing time delay $t_2 = 0$. Then, the ESE third-order response function \mathcal{S}_2 can be written as,

$$\mathcal{S}_2(\omega_1, t_2, \omega_3) = G_R^*(-\omega_1, t_2) G_R(\omega_3, t_2). \quad (22)$$

The GSB process R_3 can be analyzed in the exactly same way. We find the expressions, $R_3(t_1, t_2, t_3) = G^*(t_1) G(t_3)$ and

$$\mathcal{S}_3(\omega_1, t_2, \omega_3) = G_R^*(-\omega_1) G_R(\omega_3). \quad (23)$$

The absence of the mixing time (t_2) dependence in the expressions is easy to understand from Fig. 1(c): the system returns to the initial configuration between the second and third pulses and therefore does not evolve during the mixing time delay.

By adding the two contributions \mathcal{S}_2 and \mathcal{S}_3 , $\mathcal{S} = \mathcal{S}_2 + \mathcal{S}_3$, we arrive at one of the key results of our work,

$$\mathcal{S}(\omega_1, t_2, \omega_3) = \sum_{nm} \frac{Z^{(n)} Z^{(m)}}{(-\omega_1)^- - \mathcal{E}^{(n)}} \frac{1 + e^{i[\mathcal{E}^{(n)} - \mathcal{E}^{(m)}]t_2}}{\omega_3^+ - \mathcal{E}^{(m)}}, \quad (24)$$

where $(-\omega_1)^- \equiv -\omega_1 - i0^+$. It is readily seen that the 2DCS spectrum satisfies the relation,

$$\mathcal{S}(\omega_1, t_2, \omega_3) = \mathcal{S}^*(-\omega_3, t_2, -\omega_1). \quad (25)$$

Therefore, the amplitude and the real part of the 2DCS spectrum are both symmetric, upon the replacements $-\omega_1 \rightarrow \omega_3$ and $-\omega_3 \rightarrow \omega_1$.

We would like to emphasize that the symmetric 2DCS spectrum is rooted in two facts. First, the excitation pulse creates or annihilates electron-hole pairs at essen-

tially zero momentum²⁵. The electron-hole pairs can be either tightly bound (i.e., excitons considered in this work) or loosely bound. On the other hand, we must only take into account one electron-hole pair in the intermediate excited states. The existence of the pair-pair correlation, for example, the exciton-exciton scattering will redistribute the exciton momentum and then lead to the contributions from the excited Fermi sea $|\vec{\kappa}_\nu\rangle$. In this case, we can no longer write the response function R_2 and R_3 into a product of two polaron Green functions, i.e., as given in Eq. (15).

B. Connection to the Fermi golden rule

At this point, it is useful to contrast our simple expression of the 2DCS spectrum, Eq. (24), with the many-body formalism used by Tempelaar and Berkelbach (TB)¹⁵,

$$\mathcal{S}_{\text{TB}}(\omega_1, t_2, \omega_3) = -(2\pi)^2 \sum_{\alpha\beta} \left| \langle \Psi^i | \hat{V} | \Psi^\alpha \rangle \right|^2 \left| \langle \Psi^i | \hat{V} | \Psi^\beta \rangle \right|^2 e^{-(i\omega_{\alpha\beta} + \gamma_{\alpha\beta})t_2} \Gamma^*(E^\alpha - E^i + \omega_1) \Gamma(E^\beta - E^i - \omega_3), \quad (26)$$

where Ψ^i is the initial state, Ψ^α (Ψ^β) are the excited states with energies E^α (E^β), $\omega_{\alpha\beta} \equiv E^\alpha - E^\beta$ are the energy differences, and $\gamma_{\alpha\beta}$ are the associated decoherence rates. $\Gamma(\omega) = 1/(i\omega - \sigma)$ is the complex lineshape function with σ as the line-broadening parameter.

It is readily seen that the t_2 -independent term (i.e., the R_3 contribution) in our Eq. (24) is absent in the TB formalism. This is simply because Tempelaar and Berkelbach focused on the simulated emission signal¹⁵, which is precisely our ESE contribution \mathcal{S}_2 . We can clearly see that, if we neglect the phenomenological decoherence rates $\gamma_{\alpha\beta}$ and line-broadening parameter σ , the TB formalism Eq. (26) is essentially identical to our Eq. (20), owing to the correspondences in the indices $\alpha \leftrightarrow n$ and $\beta \leftrightarrow m$, in the overlaps $Z^{(n)} \leftrightarrow \left| \langle \Psi^i | \hat{V} | \Psi^\alpha \rangle \right|^2$ and $Z^{(m)} \leftrightarrow \left| \langle \Psi^i | \hat{V} | \Psi^\beta \rangle \right|^2$, and finally in the energies $\mathcal{E}^{(n)} \leftrightarrow E^\alpha - E^i$ and $\mathcal{E}^{(m)} \leftrightarrow E^\beta - E^i$. Thus, our derivation of the 2DCS spectrum Eq. (24) provides a useful microscopic explanation to the TB formalism Eq. (26).

C. 2DCS versus 2D Ramsey spectroscopy

Let us now briefly compare 2DCS with another type of 2D spectroscopy with ultracold atoms, the so-called 2D Ramsey spectroscopy^{28,29}, in which the exciton in 2DCS is replaced by a spin-1/2 impurity atom. The spin state of the impurity can be controlled by a rf pulse with a specific phase²⁷ and only the spin-up impurity experiences

an interaction potential with the background Fermi sea. As a result, the two spin-flip operations, given by the Pauli matrices $\hat{s}^+ = (\sigma_x + i\sigma_y)/2$ and $\hat{s}^- = (\sigma_x - i\sigma_y)/2$, roughly correspond to the exciton creation operator X^\dagger and annihilation operator X . A notable difference is that the excitation rf pulse does not change the external spatial status of the impurity atom, so it might be understood as an *effective* light-matter interaction operator $\hat{V}_{\text{eff}} \sim \sum_{\mathbf{k}} (X_{\mathbf{k}} + X_{-\mathbf{k}}^\dagger)$. Therefore, as the momentum of the impurity atom (i.e., an effective exciton) is not restricted to zero, for the intermediate many-body dynamics the excited Fermi sea with multiple-particle-hole excitations (as described by $|\vec{\kappa}_\nu\rangle$ with $\nu \geq 1$) do make contributions to the third-order response function $\mathcal{R}^{(3)}$. The simple expression found for the 2DCS spectrum, Eq. (24), does not hold in the 2D Ramsey spectroscopy. Additional terms that make the spectroscopy asymmetric (with respect to exchange the excitation and emission energies) will appear²⁹.

Apart from this difference, there are amazing similarities between the 2DCS and the 2D Ramsey spectroscopy, although in the latter^{28,29} we have used different notations such as (τ, T, t) for various time delays and (ω_τ, ω_t) as the excitation and emission energies. In both spectroscopes, phase cycling techniques can be implemented to select the desired pathways. In the rephasing mode, the ESE term $R_2(t_1, t_2, t_3)$ in the 2DCS is exactly given by the pathway $I_1^*(\tau, T, t)$ in the 2D Ramsey spectroscopy²⁹ and the GSB term $R_3(t_1, t_2, t_3)$ corresponds to the pathway $I_2^*(\tau, T, t)$ ²⁹. Finally, the third-order response function $\mathcal{S}(\omega_1, t_2, \omega_3)$ in the 2DCS precisely corresponds to

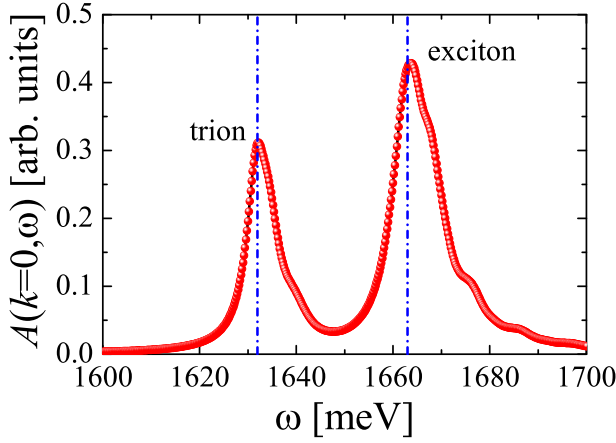


FIG. 2. The simulated polaron spectral function at the electron Fermi energy $\varepsilon_F = 11.8$ meV, revealing the existence of attractive polaron (trion) and repulsive polaron (exciton). The two dashed lines indicates the two peak positions for trions (1632 meV) and excitons (1663 meV) shown in the experimental photoluminescence spectrum of monolayer MoSe₂ taken at 20 K¹².

the symmetric 2D Ramsey response $\mathcal{A}_s^*(-\omega_\tau, T, \omega_t)$ ²⁹.

IV. RESULTS AND DISCUSSIONS

A. Computation details

To demonstrate the usefulness of the simple expression Eq. (24), we perform numerical simulations for monolayer MoSe₂, with the effective polaron model Hamiltonian in Eq. (1). To reduce the numerical workload, we load the system, which consists of N electrons and a single exciton, onto a two-dimensional square lattice with $L \times L$ sites. The electron density is then given by $n = N/(La)^2$, where a is the lattice spacing and will be set to be unity ($a = 1$) unless specified otherwise. We assume the electrons and the exciton move on the lattice with hopping strength t_c and t_d , respectively. Their single-particle energy dispersion relations are

$$\epsilon_{\mathbf{k}} = -2t_c[\cos(k_x) + \cos(k_y)] \simeq -4t_c + \frac{k_x^2 + k_y^2}{2m_e}, \quad (27)$$

$$\epsilon_{\mathbf{k}}^I = -2t_d[\cos(k_x) + \cos(k_y)] \simeq -4t_d + \frac{k_x^2 + k_y^2}{2m_X}, \quad (28)$$

where $m_e \equiv 1/(2t_c a^2)$ and $m_X \equiv 1/(2t_d a^2)$ in the dilute limit ($n \rightarrow 0$) that of interest. We note that, the momentum \mathbf{k} on the lattice takes the values,

$$(k_x, k_y) = \left(\frac{2\pi n_x}{L}, \frac{2\pi n_y}{L} \right), \quad (29)$$

with the integers $n_x, n_y = -L/2 + 1, \dots, -1, 0, 1, \dots, L/2$.

We solve the polaron model at zero temperature, by applying the polaron ansatz Eq. (16) truncated to one-particle-hole excitations³². This is the so-called Chevy ansatz³², which is known to yield a quantitatively accurate prediction for the attractive polaron energy in the strongly interacting unitary limit¹⁹. In other words, we consider a Hilbert space constructed by the two kinds of basis states (at zero polaron momentum),

$$|i\rangle = X_0^\dagger |\text{FS}\rangle, \quad (30)$$

$$|j\rangle = X_{-\mathbf{k}_p+\mathbf{k}_h}^\dagger c_{\mathbf{k}_p}^\dagger c_{\mathbf{k}_h} |\text{FS}\rangle. \quad (31)$$

Here, the Fermi sea at zero temperature $|\text{FS}\rangle$ is obtained by filling the single-particle energy level $\epsilon_{\mathbf{k}}$ with N electrons from the bottom of the energy band (i.e., $-4t_c$), up to the energy E_F . The hole momentum \mathbf{k}_h and the particle momentum \mathbf{k}_p must satisfy the constraints $\epsilon_{\mathbf{k}_p} \geq E_F$ and $\epsilon_{\mathbf{k}_h} < E_F$, respectively. The Fermi energy measured from the band bottom is then

$$\varepsilon_F = E_F + 4t_c \simeq 4\pi n t_c = \frac{4\pi N}{L^2} t_c. \quad (32)$$

It is readily seen the dimension of the Hilbert space is $D = 1 + N(L^2 - N)$. Under the basis states, the polaron Hamiltonian then is casted into a D by D matrix, with the following matrix elements,

$$\langle \text{FS} | X_0 \mathcal{H} X_0^\dagger | \text{FS} \rangle = E_{\text{FS}} - 4t_d + nU, \quad (33)$$

$$\langle \text{FS} | X_0 \mathcal{H} X_{-\mathbf{k}_p+\mathbf{k}_h}^\dagger c_{\mathbf{k}_p}^\dagger c_{\mathbf{k}_h} | \text{FS} \rangle = U/L^2, \quad (34)$$

and

$$\langle \text{FS} | c_{\mathbf{k}_h}^\dagger c_{\mathbf{k}_p} X_{-\mathbf{k}_p+\mathbf{k}_h} \mathcal{H} X_{-\mathbf{k}_p+\mathbf{k}_h}^\dagger c_{\mathbf{k}_p}^\dagger c_{\mathbf{k}_h} | \text{FS} \rangle = \left[E_{\text{FS}} + nU + \epsilon_{\mathbf{k}_p} - \epsilon_{\mathbf{k}_h} + \epsilon_{-\mathbf{k}_p+\mathbf{k}_h}^{(I)} \right] \delta_{\mathbf{k}_p \mathbf{k}_p'} \delta_{\mathbf{k}_h \mathbf{k}_h'} + \frac{U}{L^2} \left(\delta_{\mathbf{k}_h \mathbf{k}_h'} - \delta_{\mathbf{k}_p \mathbf{k}_p'} \right). \quad (35)$$

We diagonalize the matrix to obtain the eigenvalues $E^{(n)}$ and eigenstates, from which we extract the polaron energies $\mathcal{E}^{(n)} = E^{(n)} - (E_{\text{FS}} - 4t_d)$ and the residues

$Z^{(n)} \equiv \phi_0^{(n)*} \phi_0^{(n)}$. Here, due to the use of a square lattice, we also need to subtract the lowest energy of exciton (i.e., $-4t_d$) in calculating the polaron energies.

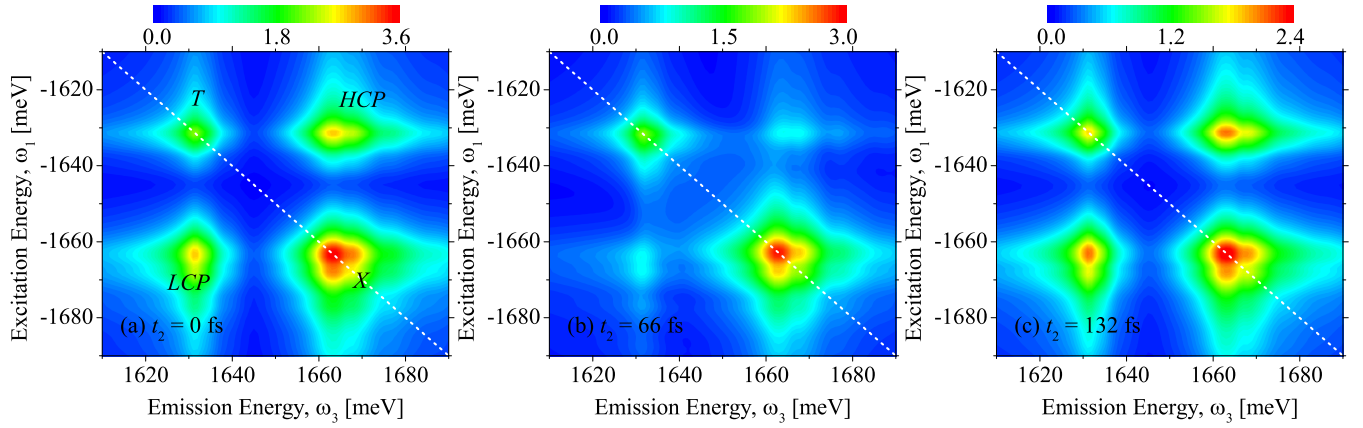


FIG. 3. The simulated rephasing 2D coherent spectra (amplitude) at various mixing time decays t_2 , to be compared with the experimental data in Fig. 2 of Ref.¹². As in the experiment, the exciton (X) and trion (T) peaks appear on the diagonal dashed line. The higher (HCP) and lower (LCP) off-diagonal crosspeaks oscillate as a function of t_2 , revealing quantum coherence between excitons and trions. The red color illustrates the maximum amplitude, as indicated in the colormap above each subplot. The electron Fermi energy is set to be $\varepsilon_F = 11.8$ meV.

Let us now fix the parameters t_c , t_d , and U in the polaron model Hamiltonian, according to the recent experimental data on monolayer MoSe₂¹². The electron mass and hole mass in MoSe₂ are very similar, i.e., $m_e = m_h \simeq 0.6m_0$ where m_0 is the free electron mass². Therefore, the mass of the exciton should be two times larger, indicating $t_d = t_c/2$. The hopping parameter t_c might be estimated by the relation $t_c = \hbar^2/(2m_e a^2)$, where the lattice spacing of monolayer MoSe₂ $a \sim 3.2\text{\AA}$ ¹⁵. We find then $t_c \sim 620$ meV. However, we can not directly use this value, considering the small electron density $n \sim 10^{12} \text{ cm}^{-2}$ in the experiment¹², which leads to $na^2 = N/L^2 \sim 10^{-3}$. Our numerical simulations have to be restricted to relatively small lattice size, i.e., $L = 16 \sim N$, which has a density $na^2 \sim 0.06$. To match the small electron density in the experiment, we need to consider a coarse-grained model by artificially enlarging the lattice spacing a (i.e., making it 10 times larger). Thus, it seems reasonable to take $t_c = 10$ meV.

To determine the interaction strength $U < 0$, we recall that the trion binding energy is about 30 meV^{12,15}. In our polaron model, this binding energy corresponds to the difference between the repulsive polaron energy and the attractive polaron energy. By performing numerical calculations with varying U at a given Fermi energy $\varepsilon_F = 11.8$ meV (which corresponds to $N = 24$ at the lattice size $L = 16$), we find that $U = -6t_c$ reproduces the observed trion binding energy, as reported in Fig. 2. There, the simulated polaron spectral function has been rigidly shifted by an amount $\omega_X = 1662$ meV, so the repulsive polaron peak lies at about 1663 meV. The photoluminescence spectrum of monolayer MoSe₂ observed in the experiment¹² is then qualitatively reproduced, by using our polaron model.

As a brief summary of the parameters to be used, throughout the work we will use $t_c = 10$ meV, $t_d = t_c/2 = 5$ meV and $U = -6t_c = -60$ meV. The lat-

tice size is fixed to $L = 16$. We tune the Fermi energy $\varepsilon_F \simeq 4\pi N t_c / L^2$ by changing the number of electrons N . To compare with the experimental 2DCS data¹², the excitation energy ω_1 and the emission energy ω_3 will be shifted by $\omega_X = 1662$ meV. As we use a finite-size square lattice, the level spacing in the single-particle dispersion relation is about $\delta = 4t_c/L$. We will use δ to replace the infinitesimal 0^+ and to eliminate the discreteness in single-particle energy levels. Finally, we would like to emphasize that, in our numerical simulations, we do not include any phenomenological parameters such as decoherence rates, which are often used to qualitatively understand the experimental data^{12,15}.

B. Quantum beats at the two crosspeaks

In Fig. 3, we present the simulated rephasing 2D coherent spectra $|\mathcal{S}(\omega_1, t_2, \omega_3)|$ at three mixing time decays $t_2 = 0$ (a), $t_2 = 66$ fs (b) and $t_2 = 132$ fs (c). Although the electron density in the experiment is unknown, we believe $\varepsilon_F = 11.8$ meV, which corresponds to the electron number $N = 24$, could be a reasonable choice. The three time delays are selected according to the measurements in Fig. 2(a)-(c) of Ref.¹², so we can make an one-to-one comparison.

We find clearly the exciton (X) and trion (T) peaks along the diagonal direction (see the dashed lines), as in the experiment. Furthermore, two off-diagonal crosspeaks, labelled as HCP and LCP , are fairly evident. Their brightness oscillates with the mixing time delay t_2 as experimentally observed, revealing the coherent coupling between excitons and trions.

All those intriguing features can be understood from the simple expression Eq. (24). At zero mixing time $t_2 = 0$, Eq. (24) precisely predicts the existence of two diagonal peaks at the attractive polaron (trion) en-

ergy $E_T = \mathcal{E}^{(n=0)}$ and at the repulsive polaron (exciton) energy E_X , respectively, with strengths given by the residues $Z_T = \phi_0^{(0)*} \phi_0^{(0)}$ and $Z_X \sim 1 - Z_T$. The expression also predicts the two off-diagonal crosspeaks at $(-\omega_1, \omega_3) = (E_T, E_X)$ and (E_X, E_T) , with strength $\sqrt{Z_T Z_X}$. At nonzero mixing time $t_2 \neq 0$, the quantum beats at the *HCP* and *LCP* crosspeaks can be easily attributed to the term $e^{-i(\mathcal{E}_n - \mathcal{E}_m)T}$, which gives rise to quantum oscillations with periodicity $2\pi/|E_X - E_T|$.

Let us now have a close comparison into the details. There is an apparent quantitative discrepancy between theory and experiment on the crosspeak brightness. Our prediction of the crosspeak strength $\sqrt{Z_T Z_X}$ means that at the zero mixing time $t_2 = 0$ the crosspeak brightness should lie between those of the two diagonal peaks, as shown in Fig. 3(a). However, this is not observed in the experiment¹². Experimentally, the crosspeaks are always darker than the two main diagonal peaks, indicating the possibility of some decoherence channels (i.e., the phonon-assisted up-conversion and down-conversion processes as experimentally observed¹²).

Apart from this discrepancy, we find a remarkable agreement between theory and experiment on other details, upon changing the mixing time t_2 . As in the experiment, in each subplot of Fig. 3, the color scale is normalized to the highest peak (i.e., the exciton peak X) in the spectra. For the trion peak T , we can see that its *relative* brightness is highest at $t_2 = 132$ fs and then is a bit weaker at $t_2 = 0$ fs and 66 fs. This subtle change is precisely observed in the experiment¹². At the two crosspeaks, their relative brightness is similar at $t_2 = 0$ fs and 132 fs, which is also experimentally observed¹².

In Fig. 4, we report the simulated rephasing 2D signal at the crosspeaks as a function of the mixing time t_2 . The amplitude of the 2D signal in Fig. 4(a) should be contrasted with Fig. 3(b) of the experiment¹². Our simulation reproduces very well the quantum oscillations observed in the experiment, with essentially the same periodicity. However, we note that, in spite of the same periodicity the two oscillations at *HCP* and *LCP* crosspeaks measured in the experiment are slightly unsynchronized. Our theory always predicts the exactly same oscillation at the two crosspeaks, as the predicted 2DCS response Eq. (24) is *symmetric* upon switching the excitation and emission energies, as we emphasized earlier.

On the other hand, the real part of the 2D signal in Fig. 4(b) might be compared with Fig. 3(b) of the pioneering work by Tempelaar and Berkelbach¹⁵. There is an excellent agreement in curve shape and periodicity. The only difference is that our 2D signal never decays to zero. This is simply due to the ground-state bleaching (GSB) process illustrated in Fig. 1(c), which has not taken into account in Ref.¹⁵ but gives an important t_2 -independent 2D signal.

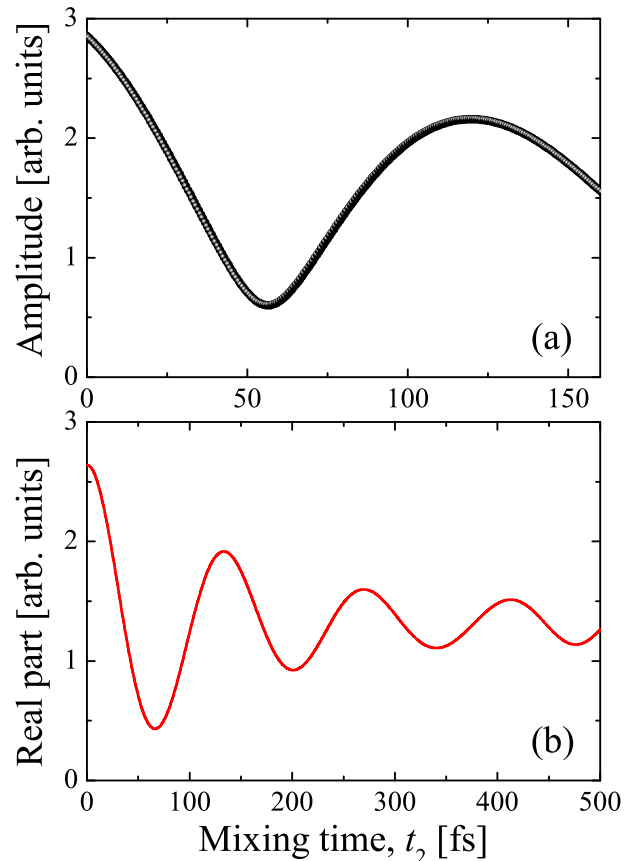


FIG. 4. The simulated amplitude (a) and real part (b) of the rephasing 2D signal at the crosspeaks as a function of the mixing time delays t_2 . The upper plot (a) is to be compared with Fig. 3(b) of the experiment¹². We take the electron Fermi energy $\varepsilon_F = 11.8$ meV.

C. Dependence on the electron density

We finally consider the dependence of the rephasing 2D signal on the electron density or the electron Fermi energy at the mixing time $t_2 = 0$. As shown in Fig. 5, as the density increases, the attractive polaron (or trions) peak acquires larger brightness (i.e., oscillation strength) and has a red-shift in energy with respect to the repulsive polaron peak (excitons). This observation agrees well the existing measurements² on the reflection (absorption) spectra of 2D materials and also the relevant theoretical explanations¹⁵. The brightness of the two off-diagonal crosspeaks also increases with increasing electron density. This theoretical prediction could be examined in future 2DCS measurements with a controllable electron density.

V. CONCLUSIONS AND OUTLOOKS

In summary, we have investigated the 2D coherent spectroscopy of excitons and trions in monolayer transition metal dichalcogenides, by using a many-body Fermi

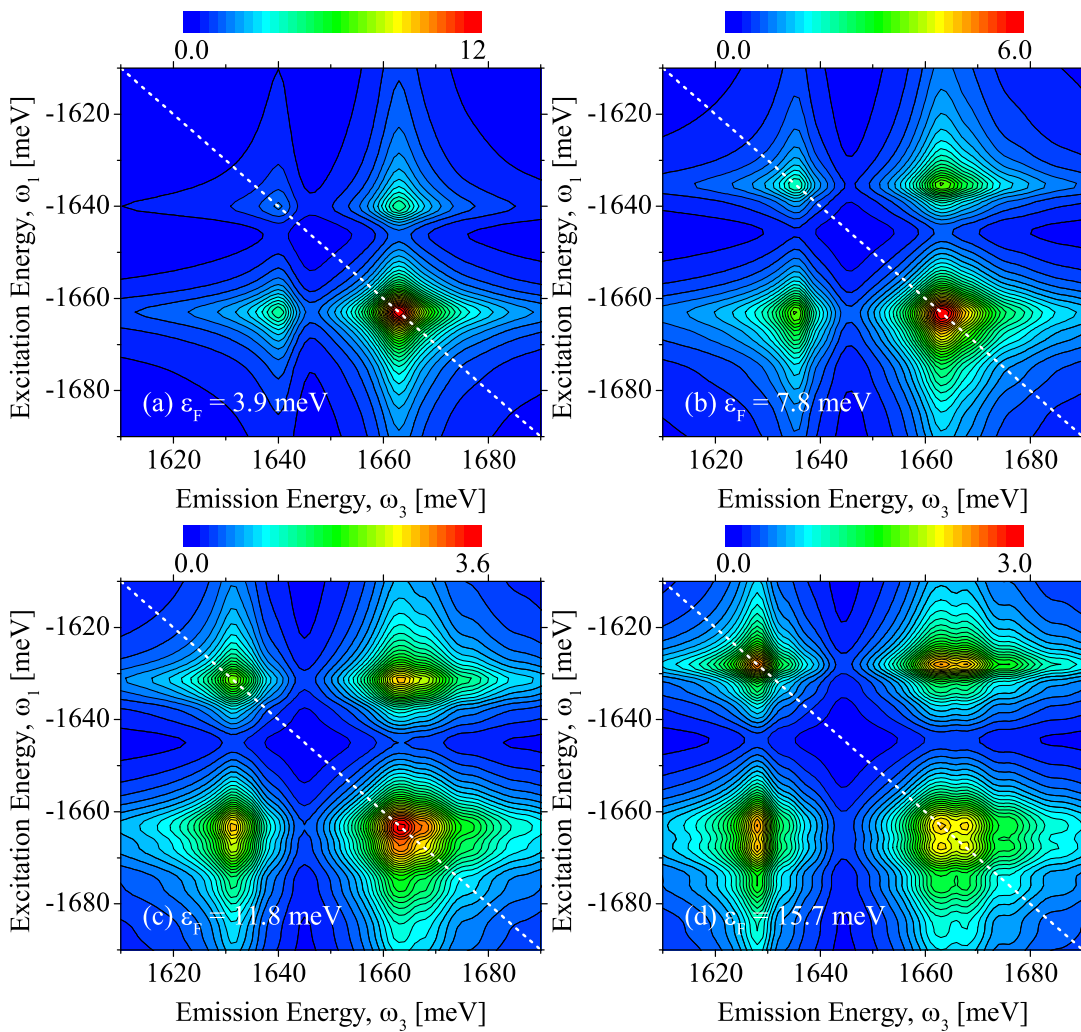


FIG. 5. The simulated rephasing 2D coherent spectra (amplitude) with increasing electron density or Fermi energy, at zero mixing time delay $t_2 = 0$. The red color illustrates the maximum amplitude, as indicated in the colormap above each subplot.

polaron model with mobile exciton. Our investigation complements the previous pioneering studies based on either few-body calculations¹⁵ or the exact solutions in immobile heavy exciton limit¹⁶. We have derived a simple expression for the 2D coherent spectroscopy, which is applicable to the limit of a single exciton. By performing numerical simulations without any phenomenological parameters, we have found that this simple expression captures the essential features of the observed 2D coherent spectroscopy of monolayer MoSe₂ and yields an excellent agreement with the experiment¹².

There are residual discrepancies at the quantitative level. For example, the predicted crosspeak relative brightness is higher than what has been observed¹² and our theory is unable to explain the slightly unsynchronized quantum beats at different crosspeaks in the experiment¹². Presumably, we feel that the polaron-polaron interaction (that we have neglected in our treatment) could be one of the sources for these discrepancies. To take into account the polaron-polaron inter-

action, we need to consider at least two excitons. The third rephasing process of excited-state absorption (i.e., the $R_1^*(t_1, t_2, t_3)$ term) then would make an important contribution.

On the other hand, experimentally, the different implementation of the polarization of the laser pulses (such as the pathway $\sigma^+\sigma^-\sigma^+\sigma^-$) can be used to create bi-excitons¹³ and bi-polarons¹⁴ in the many-body dynamics of monolayer 2D materials. It would be interesting to extend our theoretical framework to explain the experimental data in those situations.

ACKNOWLEDGMENTS

This research was supported by the Australian Research Council's (ARC) Discovery Program, Grants No. DE180100592 and No. DP190100815 (J.W.), and Grant No. DP180102018 (X.-J.L.).

- ¹ K. S. Novoselov, D. Jiang, F. Schedin, T. J. Booth, V. V. Khotkevich, S. V. Morozov, and A. K. Geim, Two-dimensional atomic crystals, *Proc. Natl. Acad. Sci. U.S.A.* **102**, 10451 (2005).
- ² G. Wang, A. Chernikov, M. M. Glazov, T. F. Heinz, X. Marie, T. Amand, and B. Urbaszek, Colloquium: Excitons in atomically thin transition metal dichalcogenides, *Rev. Mod. Phys.* **90**, 021001 (2018).
- ³ T. C. Berkelbach and D. R. Reichman, Optical and Excitonic Properties of Atomically Thin Transition-Metal Dichalcogenides, *Annu. Rev. Condens. Matter Phys.* **9**, 379 (2018).
- ⁴ K. F. Mak, C. Lee, J. Hone, J. Shan, and T. F. Heinz, Atomically Thin MoS_2 : A New Direct-Gap Semiconductor, *Phys. Rev. Lett.* **105**, 136805 (2010).
- ⁵ H. R. Gutiérrez, N. Perea-Lopez, A. L. Elías, A. Berkdemir, B. Wang, R. Lv, F. Lopez-Urías, V. H. Crespi, H. Terrones, and M. Terrones, Extraordinary room-temperature photoluminescence in triangular WS_2 monolayers, *Nano Lett.* **13**, 3447 (2013).
- ⁶ S. Ahmed, X. Jiang, F. Zhang, and H. Zhang, Pump-probe micro-spectroscopy and 2D materials, *J. Phys. D: Appl. Phys.* **53**, 473001 (2020).
- ⁷ L. B. Tan, O. Cotlet, A. Bergschneider, R. Schmidt, P. Back, Y. Shimazaki, M. Kroner, and A. Imamoglu, Interacting Polaron-Polaritons, *Phys. Rev. X* **10**, 021011 (2020).
- ⁸ K. Hao, G. Moody, F. Wu, C. K. Dass, L. Xu, C.-H. Chen, L. Sun, M.-Y. Li, L.-J. Li, A. H. MacDonald, and X. Li, Direct measurement of exciton valley coherence in monolayer WSe_2 , *Nat. Phys.* **12**, 677 (2016).
- ⁹ D. Jonas, Two-Dimensional Femtosecond Spectroscopy, *Ann. Rev. Phys. Chem.* **54**, 425 (2003).
- ¹⁰ X. Li, T. Zhang, C. N. Borca, and S. T. Cundiff, Many-Body Interactions in Semiconductors Probed by Optical Two-Dimensional Fourier Transform Spectroscopy, *Phys. Rev. Lett.* **96**, 057406 (2006).
- ¹¹ M. Cho, Coherent Two-Dimensional Optical Spectroscopy, *Chem. Rev.* **108**, 1331 (2008).
- ¹² K. Hao, L. Xu, P. Nagler, A. Singh, K. Tran, C. K. Dass, C. Schuller, T. Korn, X. Li, and G. Moody, Coherent and incoherent coupling dynamics between neutral and charged excitons in monolayer MoSe_2 , *Nano Lett.* **16**, 5109 (2016).
- ¹³ K. Hao, J. F. Specht, P. Nagler, L. Xu, K. Tran, A. Singh, C. K. Dass, C. Schuller, T. Korn, M. Richter, A. Knorr, X. Li, and G. Moody, Neutral and charged inter-valley biexcitons in monolayer MoSe_2 , *Nat. Commun.* **8**, 15552 (2017).
- ¹⁴ J. B. Muir, J. Levinsen, S. K. Earl, M. A. Conway, J. H. Cole, M. Wurdack, R. Mishra, D. J. Ing, E. Estrecho, Y. Lu, D. K. Efimkin, J. O. Tollerud, E. A. Ostrovskaya, M. M. Parish, and J. A. Davis, Exciton-polaron interactions in monolayer WS_2 , *arXiv:2206.12007* (2022).
- ¹⁵ R. Tempelaar and T. C. Berkelbach, Many-body simulation of two-dimensional electronic spectroscopy of excitons and trions in monolayer transition metal dichalcogenides, *Nat. Commun.* **10**, 3419 (2019).
- ¹⁶ L. P. Lindoy, Y.-W. Chang, and D. R. Reichman, Two-dimensional spectroscopy of two-dimensional materials, *arXiv:2206.01799* (2022).
- ¹⁷ M. Sidler, P. Back, O. Cotlet, A. Srivastava, T. Fink, M. Kroner, E. Demler, and A. Imamoglu, Fermi polaron-polaritons in charge-tunable atomically thin semiconductors, *Nat. Phys.* **13**, 255 (2017).
- ¹⁸ D. K. Efimkin and A. H. MacDonald, Many-body theory of trion absorption features in two-dimensional semiconductors, *Phys. Rev. B* **95**, 035417 (2017).
- ¹⁹ P. Massignan, M. Zaccanti, and G. M. Bruun, Polarons, dressed molecules and itinerant ferromagnetism in ultracold Fermi gases, *Rep. Prog. Phys.* **77**, 034401 (2014).
- ²⁰ R. Schmidt, M. Knap, D. A. Ivanov, J.-S. You, M. Cetina, and E. Demler, Universal many-body response of heavy impurities coupled to a Fermi sea: a review of recent progress, *Rep. Prog. Phys.* **81**, 024401 (2018).
- ²¹ J. Wang, X.-J. Liu, and H. Hu, Exact Quasiparticle Properties of a Heavy Polaron in BCS Fermi Superfluids, *Phys. Rev. Lett.* **128**, 175301 (2022).
- ²² J. Wang, X.-J. Liu, and H. Hu, Heavy polarons in ultracold atomic Fermi superfluids at the BEC-BCS crossover: Formalism and applications, *Phys. Rev. A* **105**, 043320 (2022).
- ²³ G. D. Mahan, Excitons in Metals: Infinite Hole Mass, *Phys. Rev.* **163**, 612 (1967).
- ²⁴ P. Nozières and C. T. De Dominicis, Singularities in the X-Ray Absorption and Emission of Metals. III. One-Body Theory Exact Solution, *Phys. Rev.* **178**, 1097 (1969).
- ²⁵ G. D. Mahan, *Many-Particle Physics* (Springer India, 3rd edition, January 1, 2008), Chapter 9.
- ²⁶ P. W. Anderson, Infrared Catastrophe in Fermi Gases with Local Scattering Potentials, *Phys. Rev. Lett.* **18**, 1049 (1967).
- ²⁷ M. Knap, A. Shashi, Y. Nishida, A. Imambekov, D. A. Abanin, and E. Demler, Time-Dependent Impurity in Ultracold Fermions: Orthogonality Catastrophe and Beyond, *Phys. Rev. X* **2**, 041020 (2012).
- ²⁸ J. Wang, Multidimensional Spectroscopy of Time-Dependent Impurities in Ultracold Fermions, *arXiv:2207.10501* (2022).
- ²⁹ J. Wang, H. Hu, and X.-J. Liu, Two-dimensional spectroscopic diagnosis of quantum coherence in Fermi polarons, *arXiv:2207.14509* (2022).
- ³⁰ S. Mukamel, *Principles of nonlinear optical spectroscopy* (Oxford University Press, 1995).
- ³¹ Tianhao Zhang, *Optical Two-Dimensional Fourier Transform Spectroscopy of Semiconductors* (PhD thesis, University of Colorado, 2008), Chapter 3.
- ³² F. Chevy, Universal phase diagram of a strongly interacting Fermi gas with unbalanced spin populations, *Phys. Rev. A* **74**, 063628 (2006).